AGU PUBLICATIONS

JGR

Journal of Geophysical Research: Oceans

RESEARCH ARTICLE

10.1002/2013JC009351

Key Points:
- Surface drifters detected an anticyclonic eddy in the central Red Sea
- The model successfully reproduced the observed eddy
- The eddy formed as geostrophic adjustment to seasonal buoyancy forcing

Correspondence to:
C. Chen,
c1chen@umassd.edu

Citation:
Chen, C., et al. (2014), Process modeling studies of physical mechanisms of the formation of an anticyclonic eddy in the central Red Sea, *J. Geophys. Res. Oceans*, *119*, 1445–1464, doi:10.1002/2013JC009351.

Received 12 AUG 2013
Accepted 4 FEB 2014
Accepted article online 11 FEB 2014
Published online 25 FEB 2014

Process modeling studies of physical mechanisms of the formation of an anticyclonic eddy in the central Red Sea

Changsheng Chen[1,2], Ruixiang Li[1,3], Larry Pratt[4], Richard Limeburner[5], Robert C. Beardsley[4], Amy Bower[4], Houshuo Jiang[5], Yasser Abualnaja[6], Qichun Xu[1], Huichan Lin[1], Xuehai Liu[1], Jian Lan[7], and Taewan Kim[8]

[1]School for Marine Science and Technology, University of Massachusetts-Dartmouth, New Bedford, Massachusetts, USA, [2]International Center for Marine Studies, Shanghai Ocean University, Shanghai, China, [3]South China Sea Marine Engineering Survey Center, The State Ocean Administration, Guangzhou, China, [4]Department of Physical Oceanography, Woods Hole Oceanographic Institution, Woods Hole, Massachusetts, USA, [5]Department of Applied Ocean Physics and Engineering, Woods Hole Oceanographic Institution, Woods Hole, Massachusetts, USA, [6]Red Sea Research Center, King Abdullah University of Science and Technology, Thuwal, Kingdom of Saudi Arabia, [7]College of Physical and Environmental Oceanography, Ocean University of China, Qingdao, China, [8]Korea Polar Research Institute, Incheon, South Korea

Abstract Surface drifters released in the central Red Sea during April 2010 detected a well-defined anticyclonic eddy around 23°N. This eddy was ~45–60 km in radius, with a swirl speed up to ~0.5 m/s. The eddy feature was also evident in monthly averaged sea surface height fields and in current profiles measured on a cross-isobath, shipboard CTD/ADCP survey around that region. The unstructured-grid, Finite-Volume Community Ocean Model (FVCOM) was configured for the Red Sea and process studies were conducted to establish the conditions necessary for the eddy to form and to establish its robustness. The model was capable of reproducing the observed anticyclonic eddy with the same location and size. Diagnosis of model results suggests that the eddy can be formed in a Red Sea that is subject to seasonally varying buoyancy forcing, with no wind, but that its location and structure are significantly altered by wind forcing, initial distribution of water stratification and southward coastal flow from the upstream area. Momentum analysis indicates that the flow field of the eddy was in geostrophic balance, with the baroclinic pressure gradient forcing about the same order of magnitude as the surface pressure gradient forcing.

1. Introduction

The surface circulation in the Red Sea is poorly observed and our present notions are based largely on models [e.g., *Eshel and Haik*, 1997; *Sofianos and Johns*, 2001, 2002, 2003] for insight. The pictures that have emerged from these studies are not consistent, but it is clear that a significant portion of the circulation is contained in long-lived eddies and small gyres. Models differ substantially in terms of particulars, most notably for the arrangement of boundary layers. However, the prevalence of eddies is consistent with circulation patterns deduced by *Quadfasel and Baunder* [1993] from geostrophic calculations based on limited hydrography. Our work will examine the properties and formation mechanism of one such eddy as described by recent observations.

In 2010, as one component of the Woods Hole Oceanographic Institution (WHOI) and King Abdullah University of Science and Technology (KAUST) joint research program, 29 Davis-type satellite-tracked surface drifters were deployed in the northeastern Red Sea (between 20°N and 28°N) (Figure 1) during the period 17–29 March (http://www.whoi.edu/science/PO/coastal/Redsea/) and tracked continuously for 5 months. Trajectories of these drifters strongly suggested a well-defined anticyclonic eddy, which appeared in March between 22°N and 24°N, and which became strongest in April (Figure 2). Drifters, which either stayed on the eastern shelf or crossed isobaths to enter the western shelf, tended to move along local isobaths, forming northward and southward coastal currents on the eastern and western shelves, respectively. The structure of the eddy and coastal currents can be viewed more clearly in the flow field constructed by averaging the drifter-derived Lagrangian velocities in 0.25° latitude-longitude boxes (Figure 2, bottom left) over the entire drifter-tracking period. The eddy was bounded by the shelf break, with a swirl velocity of ~0.5 m/s near the surface. The eastern portion of the anticyclonic flow was also evident on velocity profiles measured on a cross-isobath ADCP/CTD survey transect (shown in Figure 1) during 26–27 March, 2010 (Figure 3).

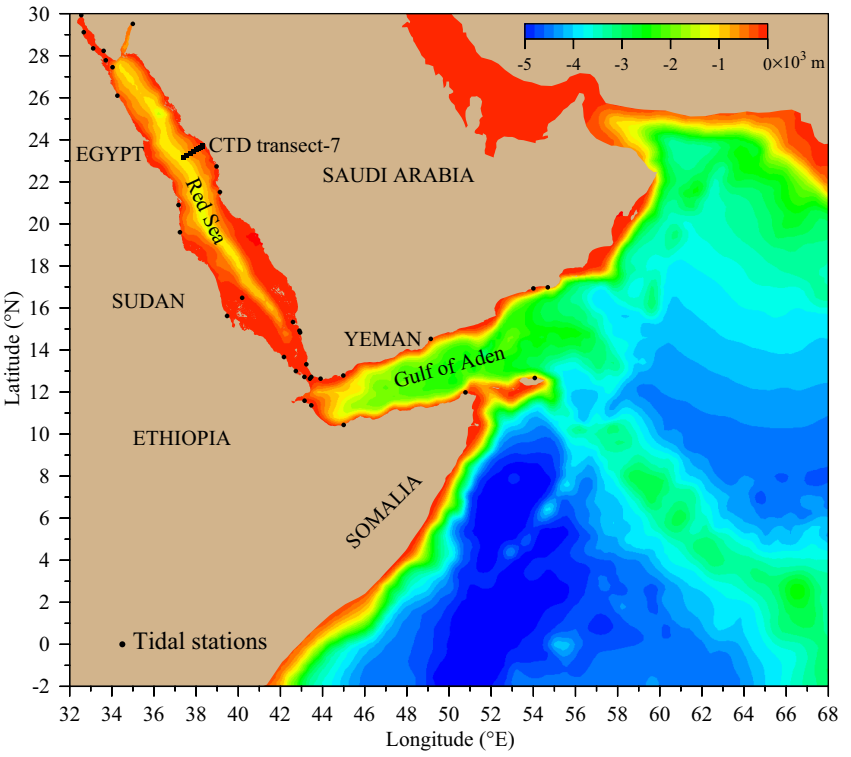

Figure 1. Geometry of the Red Sea. Colors: bathymetry (unit: 10^3 m); dots: locations of tidal gauges; and diamonds: the CTD transect-7 taken on the 26–27 March 2010 survey.

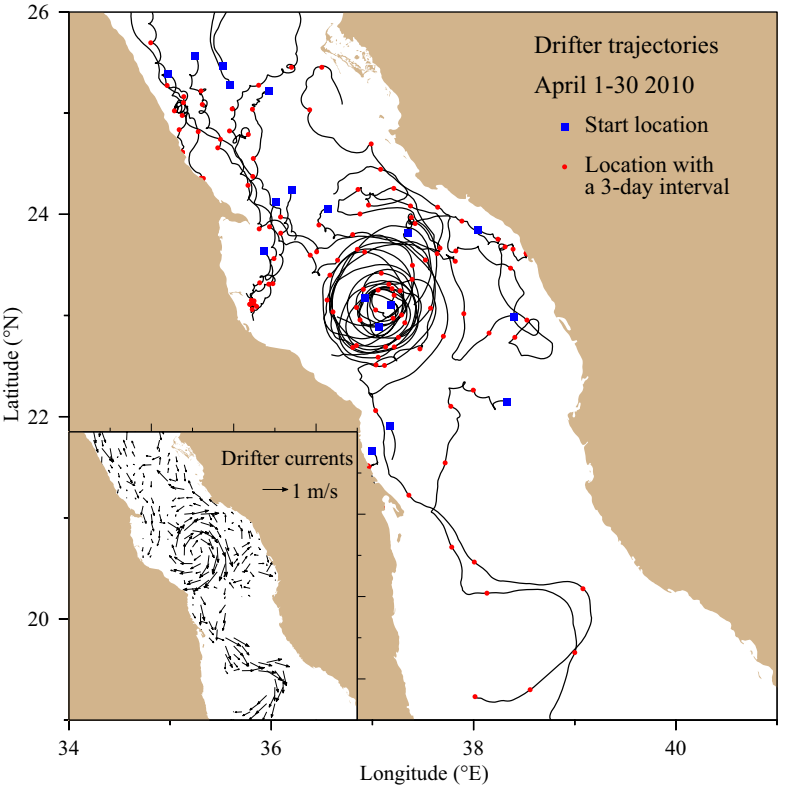

Figure 2. Trajectories of surface drifters over the period 1–30 April, 2010. Blue squares: drifter locations at beginning of 1 April; red dots: drifter locations every 3 day interval. (bottom left inset) The distribution of surface currents that were calculated by averaging the Lagrangian velocities of the drifters entering 0.25° latitude-longitude boxes over the entire drifter tracking period in 2010.

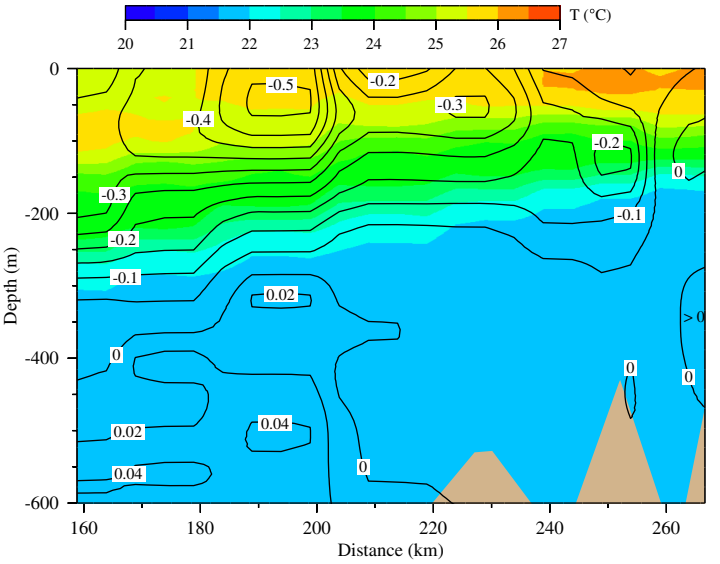

Figure 3. Cross-shelf distributions of ADCP-derived velocity (solid lines) and water temperature (colors) measured on transect-7 shown in Figure 1 during the 26–27 March 2010 ADCP/CTD survey.

In the upper 600 m, the flow was southward with a maximum speed of ~0.5 m/s near the surface. The drifter-detected anticyclonic eddy was also evident in the monthly averaged images of the altimeter-derived sea level anomaly (SLA) on April 2009 and 2010 (Figure 4). The SLA images showed that the location of this eddy varied in the vicinity each year with different magnitudes, however, the eddy was still clearly identified in the April 1999–2012 climatological mean SLA image (Figure 4). This suggested that this eddy could be a persistent mesoscale feature in this region.

What is the physical environment and what are the circumstances under which this anticyclonic eddy can form and persist? The Red Sea is a semienclosed narrow regional basin that connects to the Gulf of Aden through the constricted Bab el Mandeb (BAM) Strait. Previous field measurements were made in or near the BAM Strait, with an aim at investigating the water exchange between the Red Sea and the Gulf of Aden [e.g., *Maillard and Soliman*, 1986; *Pratt et al.*, 1999, 2000; *Beal et al.*, 2000; *Bower et al.*, 2000, 2002, 2005; *Sofianos and Johns*, 2002; *Matt and Johns*, 2007]. Due to the lack of spatial coverage of direct current measurements, however, our understanding of the dynamical character of the Red Sea circulation has been built on theoretical analyses and modeling experiments [*Phillips*, 1966; *Assaf and Anati*, 1974; *Tragou and Garrett*, 1997; *Tragou et al.*, 1999; *Eshel and Haik*, 1997; *Sofianos and Johns*, 2003; *Özgökmen et al.*, 2003; *Jiang et al.*, 2009; *Trommer et al.*, 2010]. These studies consistently suggest that the Red Sea circulation is driven predominantly by seasonal buoyancy fluxes. Recent three-dimensional modeling experiments made by *Sofianos and Johns* [2003] suggest that as a result of dynamical adjustment to the meridional pressure gradient, the central Red Sea is characterized by a permanent cyclonic gyre circulation superposed with multiple mesoscale eddies in the interior. The eddy field shown in Figure 2 was resolved in their model-computed near-surface circulation in both winter and summer (see Figures 4 and 5 in their paper), although the model-predicted circulation pattern on the northern area significantly differed from the drifter-derived field shown in Figure 2. A similar three-dimensional model experiment was also made by *Eshel and Haik* [1997] under wintertime climatological forcing conditions. However, such an eddy was not present in their simulations. The models used in these experiments were different: *Sofianos and Johns* [2003] used the Miami Isopycnic Coordinate Ocean Model (MICOM), while *Eshel and Haik* [1997] employed an Ocean General Circulation Model (OGCM) [*Gent and Cane*, 1989]. Both models have the same governing equations and featured similar horizontal resolution. The difference in their capabilities of capturing the observed eddy field motivated us to conduct a process-oriented modeling experiment with the aim at investigating the key physical mechanisms for the formation of this eddy.

This paper is focused on the physical processes that contribute to the formation of the eddy observed in the 2010 drifter trajectories. The study was approached using the unstructured-grid Finite-Volume Community Ocean Model (FVCOM) [*Chen et al.*, 2003, 2006a, 2006b, 2012]. We wish to inquire whether, for given meteorological wind forcing and surface buoyancy flux, FVCOM is capable of reproducing the observed anticyclonic eddy. If yes, is the forcing mechanism predominantly wind stress or surface buoyancy flux or some combination of both? In addition, how sensitive are the eddy properties to the initial hydrographic conditions? Finally, what is the dominant momentum balance controlling the swirl of this eddy and its spatial scales?

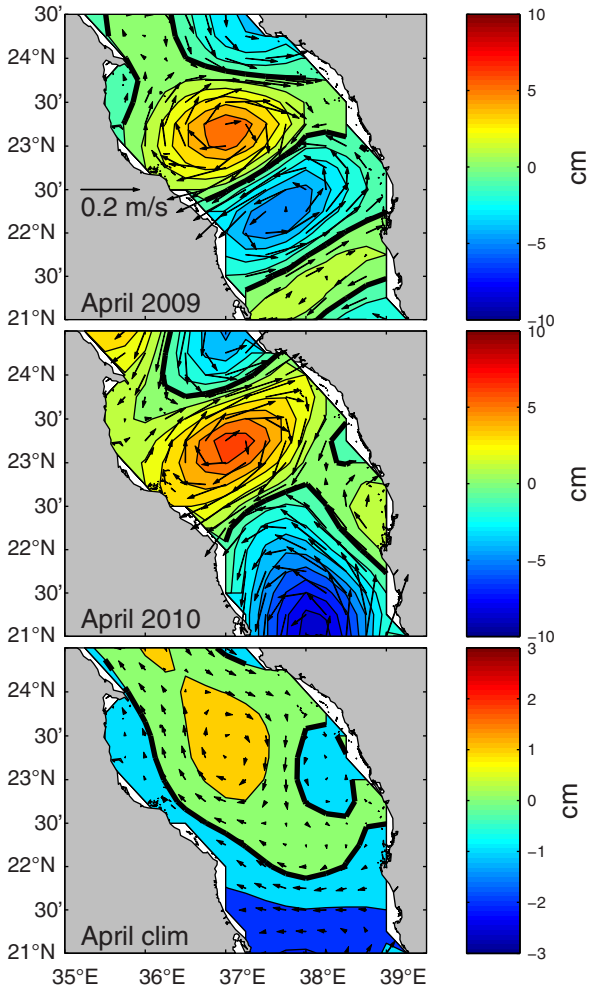

Figure 4. Images of the monthly mean altimeter-derived SLA (sea level anomaly) distribution (color shading, 1 cm contour interval) and geostrophic velocity vectors calculated using SLA; a: April 2009; b: April 2010; and c: April climatological mean for 1992–2012. Note change in color scale (but not vector scale) in (c). The data source: weekly maps from AVISO.

As our simulations will show, the eddy forms over a period of several months and within a complex environment that includes other eddies and boundary currents. It continues to exhibit time dependence after it has formed. It is difficult, therefore, to attribute its formation to a single mechanism such as baroclinic instability or spin-up over confining topography, or to write down a simple description of the step-by-step energy transfers that take place. We have therefore concentrated on identification of the characteristics of the eddy and, broadly speaking, the features that are necessary for its formation and existence.

Remaining sections of this paper are organized as follows. In section 2, FVCOM and the design of the numerical experiments are described. In section 3, results of model simulation and process-oriented experiments are presented. In section 4, comparisons are made for model results driven by different wind forcing and initial conditions. In section 5, relationships of the eddy formation to upstream flow conditions are discussed. In section 6, the conclusions are summarized.

2. The Model and Design of Numerical Experiments

The ocean model used in this study is a subdomain FVCOM configured for the Red Sea (hereafter referred to as RS-FVCOM) and nested with Global-FVCOM [*Gao et al*., 2011]. The computational domain of RS-FVCOM covered the entire Red Sea and Gulf of Aden and was enclosed by an open boundary over the western shelf of the Arabian Sea (Figure 5). The domain was discretized by a nonoverlapping triangular grid in the horizontal with resolution varying from ∼3 km near the coast to ∼8 km in the interior in the Red Sea and ∼8–50 km over the Arabian Sea shelf. Resolution is defined here as the length of the longest edge of a triangular grid cell. The design of the horizontal grid resolution was aimed at resolving the mesoscale dynamics with an internal Rossby radius of deformation of 30–40 km in the central Red Sea [*Zhai and Bower*, 2013]. The vertical grid discretization was implemented using a hybrid terrain-following coordinate with a total of 30 layers [*Chen et al*., 2012]. The *s*-coordinate was used in regions with depth greater than 90 m in which five uniform layers with a thickness of 3 m were specified near the surface and bottom, respectively. The uniform thickness σ-coordinate was employed in regions of depth less than 90 m. The coordinate transition occurred at the depth of 90 m where all layers have a uniform thickness of 3 m.

RS-FVCOM was driven by a prescribed tidal elevation at the open boundary and meteorological forcing [wind stress, net heat flux plus shortwave irradiance in the water column, and evaporation-precipitation (*E-P*)] at the sea surface. The tidal forcing was the sum of periodic functions specified by the amplitudes and phases of the eight major tidal constituents M_2 (12.42 h), N_2 (12.66 h), S_2 (12.00 h), K_2 (11.97 h), K_1 (23.93 h), O_1 (25.82 h), P_1 (24.07 h), and Q_1 (26.87 h), which have been obtained through interpolation from the *Egbert and Erofeeva*

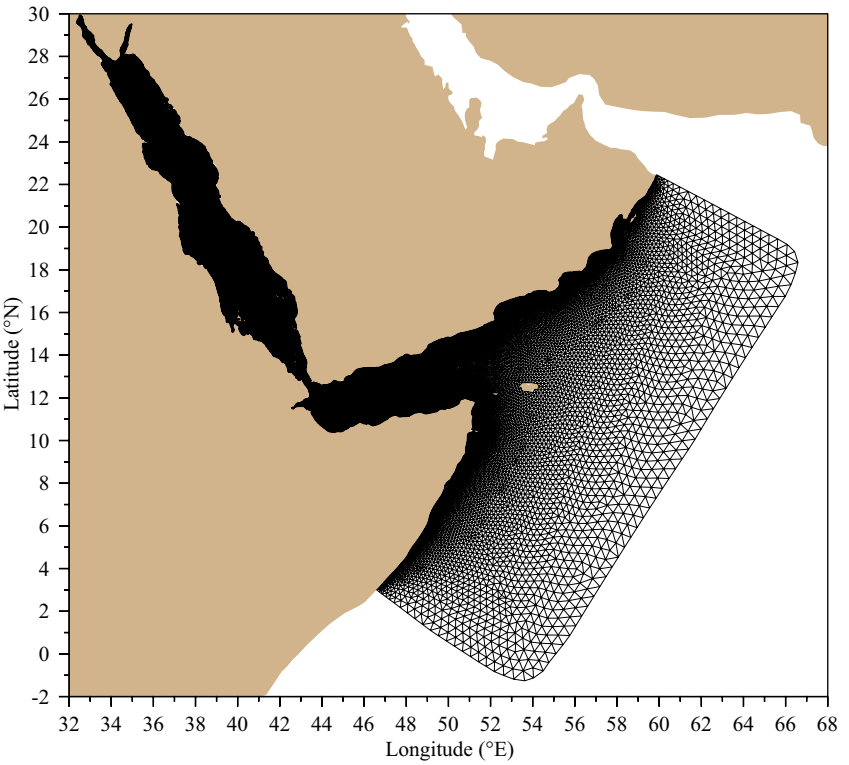

Figure 5. The unstructured triangular grid of RS-FVCOM.

[2002] 1/6° inverse tidal model results. The meteorological forcing was constructed using the 10 km high-resolution hourly Weather Research and Forecasting (WRF) fields that were produced and validated via observations by *Jiang et al*. [2009]. To examine the sensitivity of the oceanic responses to the wind forcing, we also used the 1.875°×1.875° NCEP wind field (with a 6 h time interval) to drive the model. Because the high-resolution WRF wind was only available for a period from August 2008 to October 2009, the model was spun up starting on 1 August, 2008 and continuously run until May 2009. This approach was based on (1) the suggestion that the anticyclonic eddy is likely a persistent feature since it was observed with surface drifters from March to August 2010 and in repeated hydrographic sections by *Quadfasel and Baunder* [1993] and (2) our focus on process-oriented numerical experiments rather than a real-time simulation.

The WRF-produced surface heat flux changed significantly with seasons. The ocean gained heat during spring through summer (April–August) and lost heat during fall through winter (Figure 6, top). The maximum daily gain was ~200 W/m^2, occurring in April, while the maximum daily loss could exceed 700 W/m^2, occurring in February. Evaporation was in general one order of magnitude larger than precipitation (Figure 6, bottom). The peaks of evaporation and precipitation occurred in February and November, respectively. Both hourly and 6 hourly WRF and NCEP winds varied daily and seasonally. The WRF-produced monthly averaged wind stress field was characterized by coastal mountain gap wind jets: westerly (blowing from the west) during summer and easterly (blowing from the east) during winter (Figure 7) [*Jiang et al*., 2009]. The northerly and southerly winds converged around 18°N from November through February. The southerly wind significantly weakened in March and disappeared in May through September. NCEP-produced monthly averaged wind stress fields had a similar seasonal distribution as the WRF wind stress but were generally weaker (with maximum differences up to ~0.1 N/m^2) (Figure 8). The wind imparts momentum to the water, amplifies evaporation, and contributes to vertical mixing. Since different types of wind products have been often used in previous modeling experiments [e.g., *Eshel and Haik*, 1997; *Sofianos and Johns*, 2003], using both WRF and NCEP winds to drive RS-FVCOM and compare their results provides new insights into the dynamical sensitivity of eddy simulation to wind intensity in the central Red Sea.

The extensive evaporation and seasonal heating in the Red Sea make this ocean basin strongly stratified over the entire year [*Tragou et al*., 1999; *Sofianos and Johns*, 2002]. We believe that given the same external

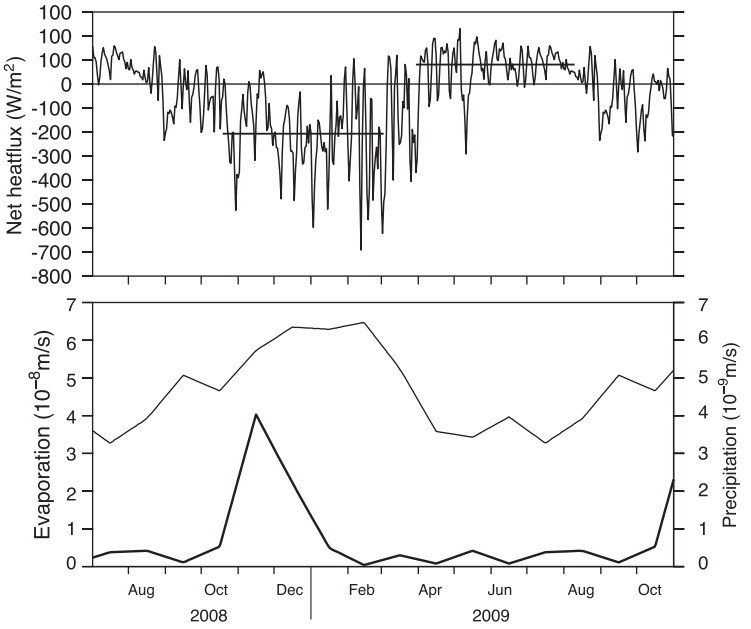

Figure 6. Time series of the WRF-computed net surface heat flux (top), evaporation (thin solid line in the bottom) and precipitation (heavy solid line in the bottom) at the center of the observed anticyclonic eddy over the time period 1 July 2008 to 1 October 2009. Heavy solid straight lines in the top are the mean values averaged over the corresponding time intervals.

meteorological and tidal forcing conditions, the model-simulated ocean circulation and stratification in the Red Sea could be influenced by the fields of water temperature (*T*) and salinity (*S*) specified as initial conditions. To investigate this issue, we ran RS-FVCOM with two types of the initial T/S conditions: (1) the 50 year Global-FVCOM spin-up field at 00:00 A.M. 1st August and (2) climatologically monthly averaged August T/S fields. The climatological field was built using the historical NODC hydrographic database and averaging over 10 km × 10 km boxes.

Before the numerical experiments for this study were made, RS-FVCOM was first validated for tidal simulation. Although the tidal elevations in the interior Red Sea are very weak, they are significant in the narrow BAM Strait and in the shallow coastal areas where numerous islands exist. The tidal rectified flow is not negligible in these regions. The comparison of model-predicted and observed tidal elevations was made on 33 tidal gauges (shown in Figure 1) with results presented in Appendix A.

RS-FVCOM was run using the mode-split FVCOM solver with a default setup of the modified Mellor and Yamada level 2.5 (MY-2.5) and Smagorinsky turbulent closure schemes for vertical and horizontal mixing, respectively [*Mellor and Yamada*, 1982; *Smagorinsky*, 1963]. The time step for the external mode was 4 s and the ratio of internal mode to external mode was 10.

3. Results of Simulation and Process-Oriented Experiments

Driven by the WRF and tidal forcing with the initial T/S conditions produced by the Global-FVCOM 50 year spin-up fields, RS-FVCOM succeeded in reproducing an anticyclonic eddy very similar to the April 2010 observations (Figure 9). The model-computed, near-surface current field showed that the southern portion of this eddy was intensified as a result of an offshore flow of coastal waters from the eastern shelf. A well-defined southward coastal flow was found on the western shelf, with a small portion entering the anticyclonic eddy around its northern edge. Although the west coast has a peninsula near 24°N, the eddy does appear to have been generated by a partial separation of the western boundary layer: in fact, the bulk of this southward flow continues to hug the coast and passes to the west of the eddy. The distribution of model-computed currents was very similar to the drifter-derived currents shown in Figure 2. In addition, the entire central Red Sea was characterized by a cyclonic gyre circulation as an adjustment of currents and meridional pressure gradients. Significant cross-isobath westward flows appeared in the northern area, contributing to intensification of the southward coastal flow on the western shelf.

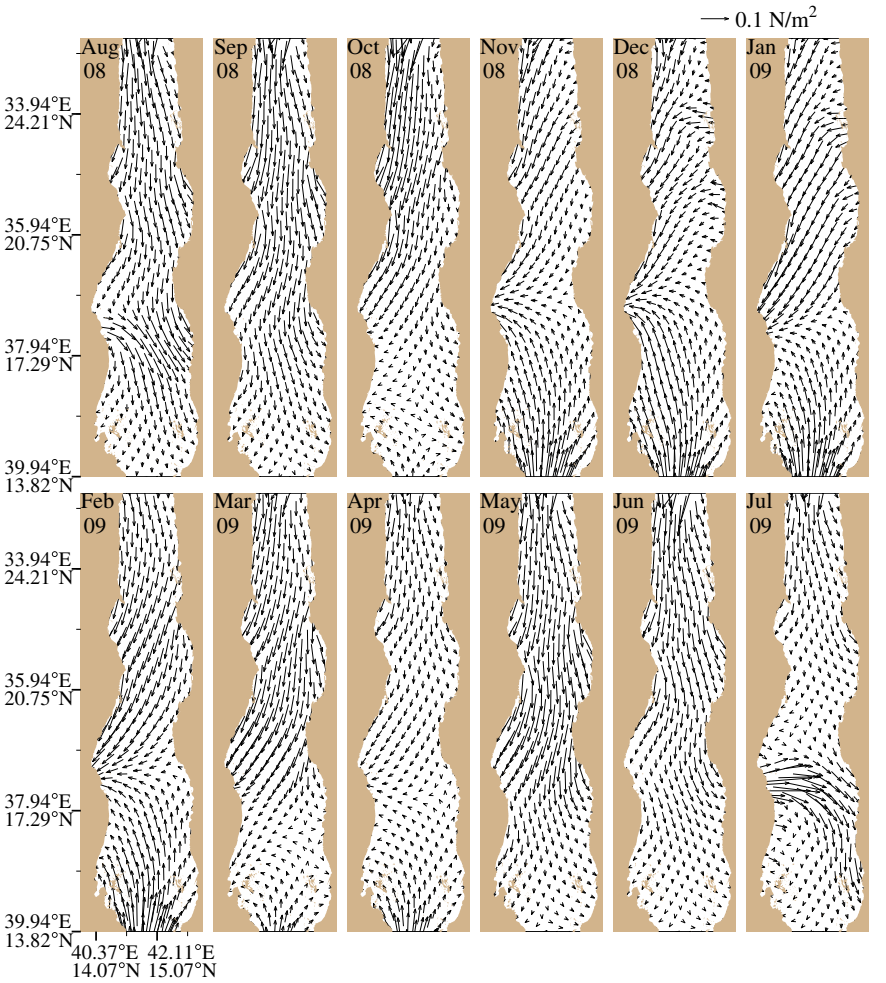

Figure 7. Distributions of the WRF-computed monthly averaged surface wind stress over the time period August 2008 to July 2009. The stress vectors were plotted with a resolution of 0.3° to make the figure visible.

The model-produced anticyclonic eddy had the same shape, diameter (~120 km), and location as the drifter-derived eddy. The model eddy was subsurface intensified with a maximum velocity of ~0.3–0.4 m/s at a depth of ~200 m (see inset in Figure 9). The Davis-type drifters were designed to measure the current with a 1 m, four-panel sail centered at a depth of ~75 cm from the surface. Assuming that the sail averages

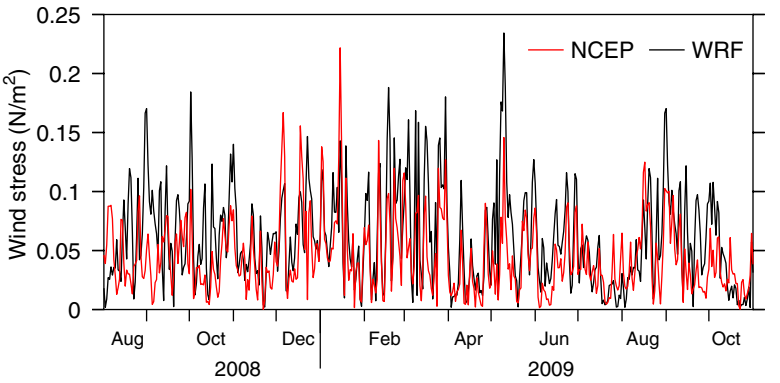

Figure 8. Time series of the surface wind stress amplitude calculated using the WRF and NCEP winds at a location in the interior around 23°N over the time period August 2008 to October 2009.

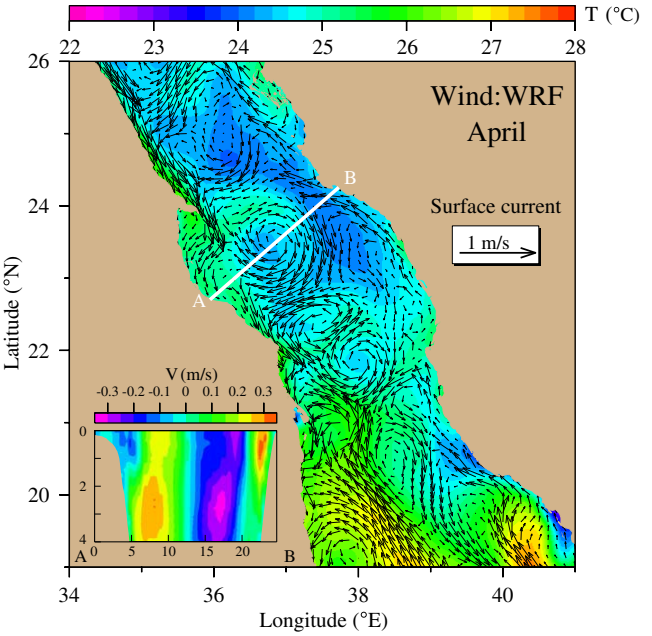

Figure 9. Distributions of RS-FVCOM-computed April monthly averaged near-surface current vectors and water temperature (colors) under the WRF wind conditions. (bottom left inset) The distribution of the velocity normal to the transect A–B with units of (×10 km) for the *x*-axis and (×10^2 m) for the *y*-axis, respectively.

the current over the vertical extent of the sails, the mean drifter-measured velocity was at the depth of 0.75 m. This is closer to the surface than the center of the top 3 m deep *s*-coordinate, assuming that the horizontal velocity was computed in the vertical center of the layer. At the measurement depth, the model-computed velocity of this eddy was weaker than the drifter-derived velocity, suggesting that the model probably overestimated vertical mixing in the interior of the central Red Sea. Such overestimation could be due to either errors in the WRF-predicted wind stress magnitude, mixing parameterization used in the turbulent closure scheme or the initial stratification. We will discuss this issue later.

The success in reproducing this eddy indicates that RS-FVCOM captured the physical processes that lead to the eddy formation. What is the key critical process: wind forcing or buoyancy flux? To address this question, we conducted four process-oriented experiments. The first experiment (named "Ex#-*a*") was made for the barotropic (constant T/S) case driven by wind forcing only, while the other experiments were made for stratified initial conditions with no wind. These include a case with the surface heat flux plus *E-P* (named "Ex#-*b*"), surface heat flux only (named "Ex#-*c*"), and by *E-P* only (named "Ex#-*d*").

In the barotropic Ex#-*a*, the wind-driven subtidal circulation in the Red Sea was characterized by narrow southward flows over the eastern and western shelves and a broad northward returned flow in the interior (Figure 10, top left). The southward flow was intensified over the western shelf with speeds of order ∼7 cm/s, and the cross-isobath scale of the returned flow was ∼130 km, with speeds of ∼0.5–1.0 cm/s below a depth of 50 m (Figure 11, top left). This circulation pattern is very similar to the dipole gyres derived by an analytical solution for a linear, homogeneous, wind-driven 3-D flow in a rotating sloping bottom basin [*Winant*, 2004]. This analytical solution can be accurately resolved by FVCOM [*Huang et al*., 2008]. The primary difference here is that the wind field over the central Red Sea featured a westward convergence, which intensified the southward flow over the western shelf shown in Figure 9 but was unable to generate an anticyclonic eddy as observed in drifter trajectories.

In Ex#-*b*, the boundary and initial conditions were the same as the simulation for a stratified case shown in Figure 9 except wind forcing was excluded. The anticyclonic eddy still existed in the same area in April, although the intensity and distribution of the coastal flow over the shelf significantly differed (Figure 10, top right). Here the southward western boundary current veered to the east, leaving the coast and wrapping around the northern portion of the eddy, then continued southward around the eastern edge of the eddy. The water temperature inside the eddy was warmer and velocity had its maximum at the surface and was relatively uniform in the upper 400 m (Figure 11, top right). Unlike the case with wind forcing and stratification (Figure 9), water in the eddy in Ex#-*b* was supplied mainly from the cyclonic eddy on its southwestern side and the southward coastal flow over the western shelf. The disappearance of the southward coastal flow in the region south of 24°N over the western shelf in this case was consistent with the result from Ex#-*a*, where the model suggested that this coastal flow formed as the result of wind forcing. With only surface heat flux plus *E-P* forcing, the entire central Red Sea was characterized by multiple eddies. The southward coastal flow found in the region north of 24°N over the western shelf was from a cyclonic eddy

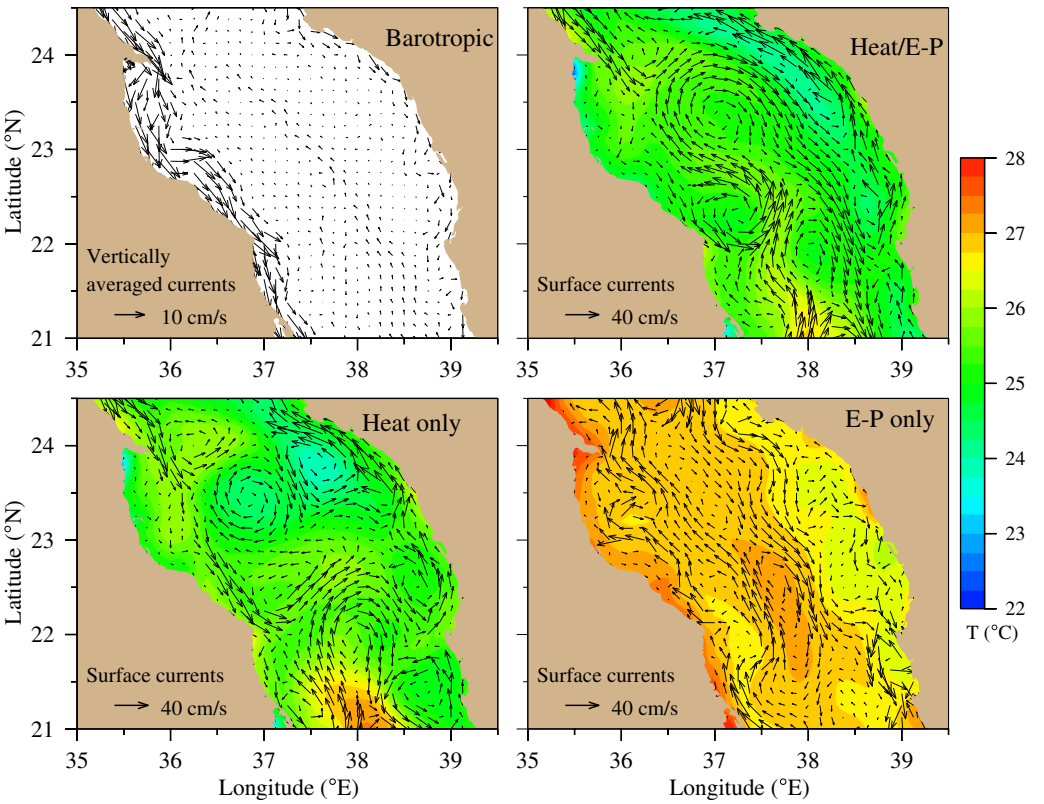

Figure 10. (top left) Distributions of April monthly mean, vertically averaged current vectors for the homogeneous model run. (top right and bottom) Distributions of April monthly averaged near-surface velocity and water temperature for the cases with only the surface heat flux plus *E-P* forcing (top right), with only surface heat flux forcing (bottom left), and with only *E-P* forcing (bottom right).

in that region. Ex#-*b* suggests that the anticyclonic eddy detected in the drifter trajectories could be generated under the forcing condition with only buoyancy forcing at the sea surface. This also means that the wind did not play a critical role in the formation of this eddy.

In Ex#-*c* and Ex#-*d*, we attempt to access the relative contribution of surface heat flux and *E-P* in the generation of observed anticyclonic eddy. Ex#-*c*, where the buoyancy flux in entirely due to heating, the eddy formed (Figures 10 and 11), though reduced in size, it retained the main characteristics found in Ex#-*b*. In Ex#-*d*, where the forcing is due entirely to E-P, there was a broad anticyclonic region in the interior, but the boundary currents reversed direction relative to the previous two experiments. The absence of cooling and the presence of evaporation have conspired to reverse the pressure gradients between the interior and shelf regions. This result is an along-slope southward flow over the eastern area and an along-slope northward flow over the western area in the central Red Sea between 22°N and 24°N (Figure 10, bottom right). The negative vorticity produced by these two flows is consistent with the anticyclonic interior region, but it is difficult to relate this aspect to the generation of the eddy in Ex#-*b*.

4. Effects of Wind Forcing and Initial Conditions

The four process-oriented experiments demonstrated that the anticyclonic eddy detected by the drifter trajectories could be formed as a result of oceanic responses to the seasonal surface heat flux in the absence of wind forcing. Although wind forcing did not play a critical role in this eddy formation, it could significantly influence the intensity and structure of this anticyclonic eddy. Wind forcing alone gave rise to a southward coastal current over the western shelf in April, and wind-induced mixing established a relatively strong thermocline below the mixed layer to form a subsurface intensification of this eddy flow. It is clear that in order to simulate or predict this anticyclonic eddy (or even the circulation in the central Red Sea),

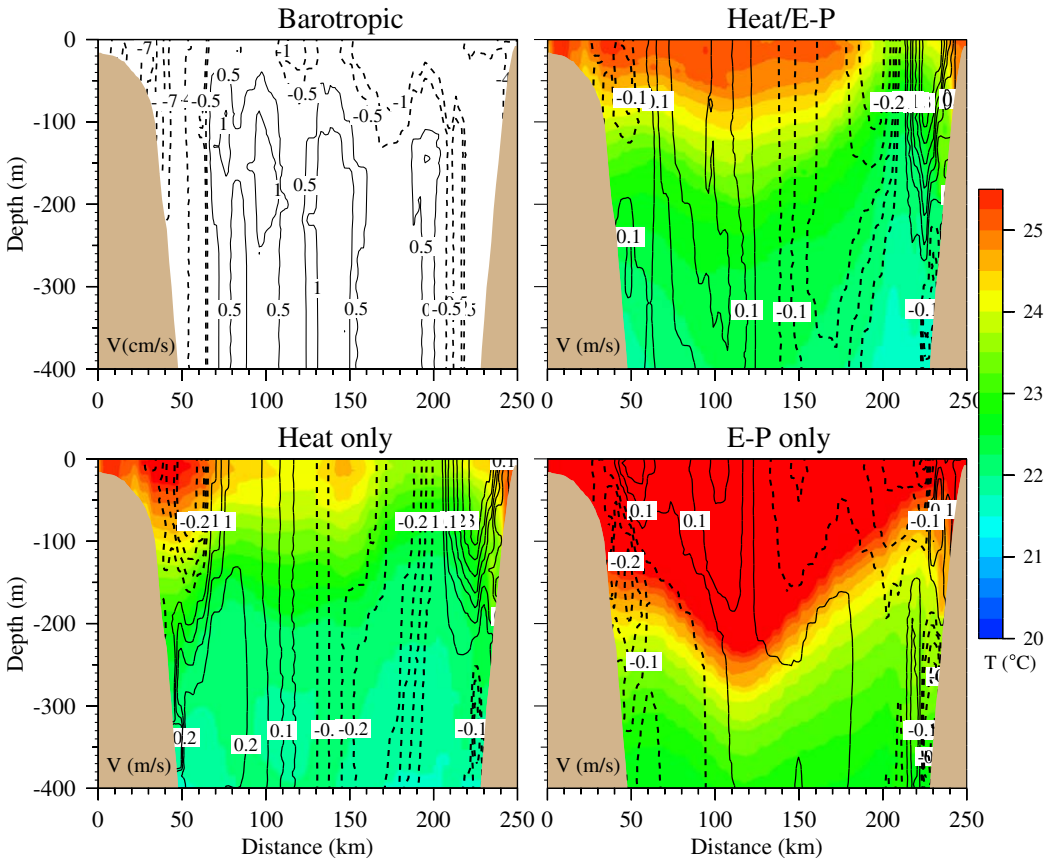

Figure 11. (top left) Distributions of April monthly mean, vertically averaged velocity on the transect A–B for the homogeneous model run. (top right and bottom) Distributions of April monthly averaged near-surface velocity and water temperature on the transect A–B for the cases with only surface heat flux plus *E-P* forcing (top right), with only surface heat flux forcing (bottom left) and with only *E-P* forcing (bottom right).

one must drive the model with realistic and accurate wind forcing. That can be seen in a comparison of model results using the WRF and NCEP winds. Keeping buoyancy forcing and initial/boundary conditions unchanged and replacing the WRF wind by the NCEP wind, the model-computed near-surface circulation in the central Red Sea (Figure 11) differed significantly from that produced by the WRF wind (Figure 9). Although the general patterns of monthly averaged WRF and NCEP winds were similar, the spatial resolution of the NCEP wind was too coarse to resolve the mesoscale variability of the wind in this narrow ocean basin. The WRF wind was generally stronger than the NCEP wind. As a result, the maximum swirl velocity of the anticyclonic eddy was at subsurface in the WRF wind case (Figure 9) but at the surface in the NCEP wind case (Figure 12). The appearance of the anticyclone in both simulations is consistent with the fact that the wind is not crucial in generating this feature. However, the eddy activity to the south is quite different in the two cases, which indicates sensitivity to the wind elsewhere [see, e.g., *Zhai and Bower*, 2013].

The importance of buoyancy flux in the eddy formation was consistent with the previous modeling results by *Sofianos and Johns* [2003], who found that "the circulation produced by the buoyancy forcing is stronger overall and dominates the wind-driven part of the circulation." In theory, the oceanic response to buoyancy forcing varies with the background stratification. In the model simulation, the background stratification refers to the initial T/S conditions specified for the model run since both water temperature and salinity initially varied significantly in space. In many shallow coastal regions where the water is vertically well mixed, the memory of the ocean current from its initial condition is about the local inertial time period [*Xue et al.*, 2011]. Since the deep region of central Red Sea is stratified and geostrophic currents satisfy the β-effect dynamics, the spatial and temporal variability of buoyancy forcing-induced stratification could differ for different initial T/S conditions after a long-term simulation. To what degree could such a difference in water

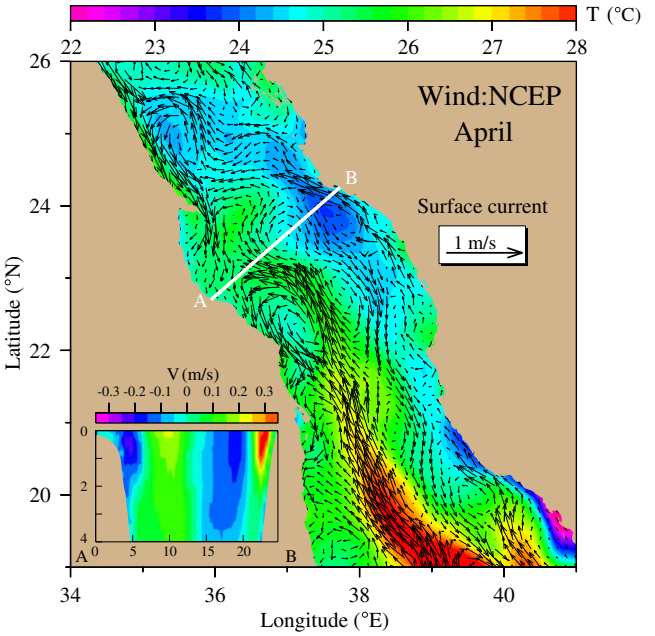

Figure 12. Distributions of RS-FVCOM-computed April monthly averaged near-surface current vectors and water temperature (colors) simulated with NCEP wind forcing. (bottom left inset) The distribution of velocity normal to the transect A–B with units of (×10 km) for the *x*-axis and (×10^2 m) for the *y*-axis, respectively.

stratification influence the formation of the anticyclonic eddy detected by drifter trajectories in the central Red Sea? We have examined this question by driving RS-FVCOM with an initial condition specified by the monthly climatological T/S field and comparing its results with those described above.

The spatial distributions of the initial T/S fields produced by the Global-FVCOM 50 year spin-up simulation and climatologically monthly averaged NODC hydrographic data significantly differed (Figure 13), especially over western and eastern shelves. The T/S contours were oriented longitudinally in the fields produced by the model spin-up results, while they were distributed transversely in the field constructed by climatological data. In the region where the water depth is greater than 100 m, both model spin-up and climatological T/S fields show

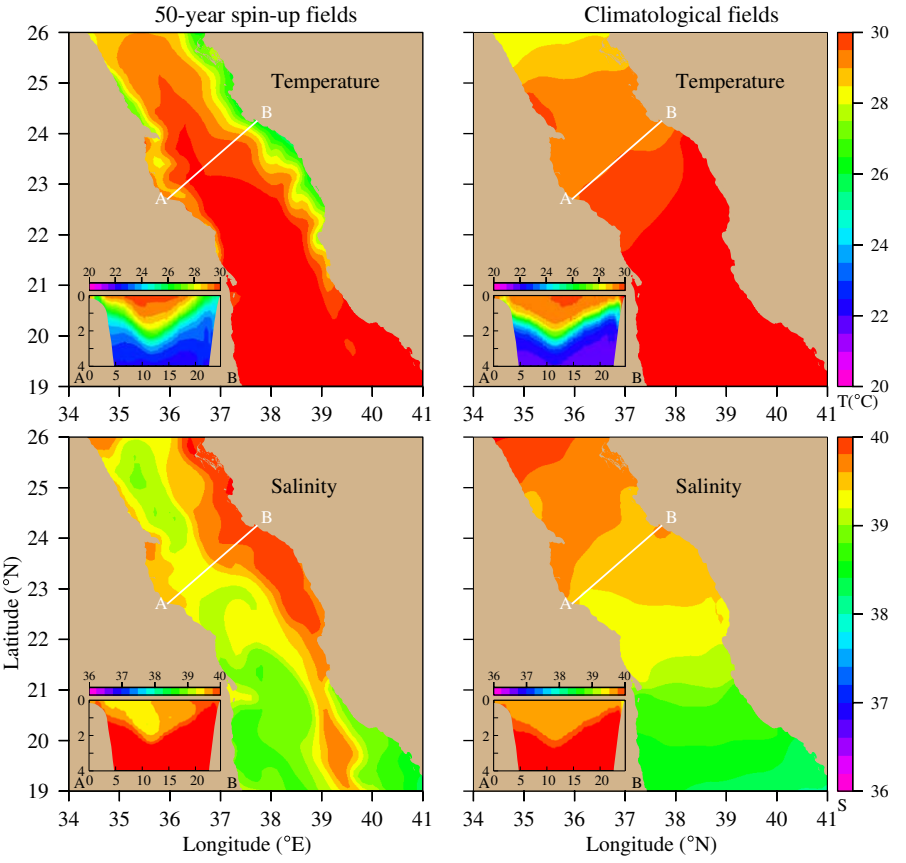

Figure 13. Distributions of near-surface temperature and salinity output from the Global-FVCOM 50 year spin-up fields at 1 July (left) and constructed by the July monthly climatologically averaged hydrographic data (right). Figures in the bottom left inset are distributions of water temperature and salinity on the transect A–B with units of (×10 km) for the *x*-axis and (×10^2 m) for the *y*-axis, respectively.

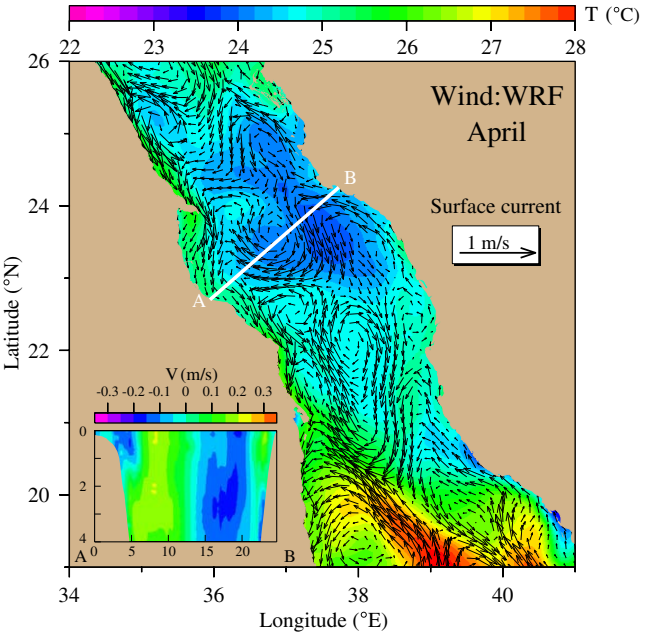

Figure 14. Distributions of RS-FVCOM-computed April monthly averaged near-surface current vectors and water temperature (colors) produced by the model run with the initial T/S field specified using the July climatological averaged data. (bottom left inset) The distribution of velocity normal to the transect A–B with units of (×10 km) for the *x*-axis and (× 10^2 m) for the *y*-axis, respectively.

similar vertical structure and cross-isobath gradients. The model-computed flow field with an initial condition specified using the climatological field (Figure 14) showed a similar general pattern as the results (Figure 9) using the Global-FVCOM 50 year spin-up field. Looking into the details, however, the flow fields produced by these two initial conditions differed significantly in the regions to the north and south of the anticyclonic eddy. In the case of the 50 year spin-up T/S initial field, the model showed more than five mesoscale eddies in the southern region, but some of these eddies were smoothed out in the case for the climatological T/S initial field. The anticyclonic circulation in the central region was much stronger in the case for the climatological T/S initial field than in the case for the 50 year spin-up T/S initial field. This difference directly affected the structure and intensity of the anticyclonic eddy observed by drifter trajectories: it was weaker in the case with the climatological T/S initial field due to the removal of the water by the cyclonic flow in the northwestern area. Despite these differences, the anticyclonic eddy observed by drifter trajectories was resolved in both cases. This fact suggests that the eddy may be more robust than the surrounding features.

5. Impacts of Upstream Flows

One question here is: could the anticyclonic eddy form as a result of short-time adjustment to water stratification in spring? To address this question, we have run a series of simulations beginning with first day of each month from December (previous year) to April. In each case, the model was driven with an initial condition set by the climatological monthly averaged T/S fields for the same month. The anticyclonic eddy was produced only for model runs beginning in December or earlier, suggesting that the eddy was not simply a result of short-term adjustment to the local change of stratification due to the surface heat flux. It is clear that the formation of this eddy is caused not only by the seasonal surface heat flux but also by the basin-scale adjustment of the flow field to the seasonal change of surface heat flux. To examine these adjustment processes, we conducted a Lagrangian particle tracking experiment in the model-predicted flow field and examined the basin-scale flow connectivity with the evolution of flow field and change of stratification over the winter-spring seasons.

To ensure that the model-computed particle-tracking trajectories are capable of representing the surface motion observed by drifters deployed in 2010, we first released neutrally buoyant surface particles at the same time and locations as the drifters in March 2010 and tracked them until the end of April. The model-computed particle trajectories show generally similar circulation patterns as those observed in the drifter trajectories, especially for particles released in the central region (Figure 15). This suggests that the model successfully captured the general circulation pattern in this region. With this result, we then released a group of particles in the northern end of the Red Sea in different months before April to determine the time required for water at the northern end to move to the area of the anticyclonic eddy. For particles released at the surface in winter, the model suggested a transit time of ~3–4 months. An example is shown in Figure 16 for the trajectory of a particle released on 10 December and tracked until 1 May. The particle slowly flowed westward in December. On 1 January, it entered the coastal flow zone and then moved

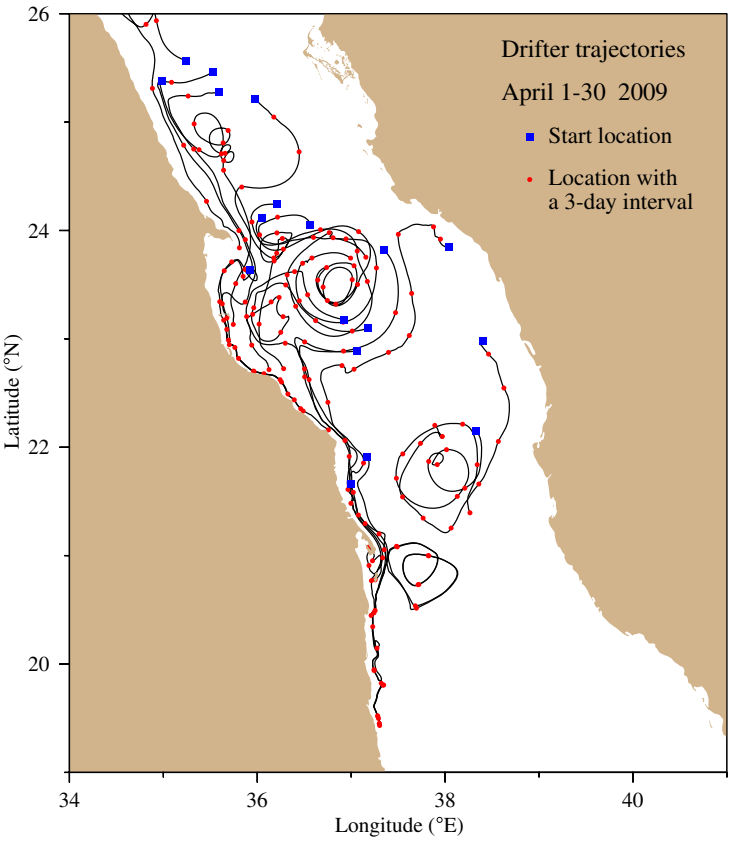

Figure 15. Trajectories of particles released at the same locations as the satellite-tracked surface drifters on 1 April. The tracking period of these particles were from 1 April to 30 April.

southward at a faster speed, arriving in the western shelf region around 25°N in early March. It entered the anticyclonic eddy field in April and drifted to the western coastal region south of 20°N in early May. This indicates that the water tracked by drifter trajectories in March and April 2010 in the Red Sea between 21°N and 26°N could have been the water that was advected southward from the northern (upstream) end during the previous winter. If this is the case, then the formation of the anticyclonic eddy observed by drifter trajectories in April was related to the water transport from upstream. This is consistent with the fact that the model was incapable of generating the observed anticyclonic eddy by short-term simulations of less than 3 months, since the flow field observed in March and April resulted not only from the oceanic response to surface heat flux and winds but also from the flow adjustment influenced by the southward coastal flow from the upstream region.

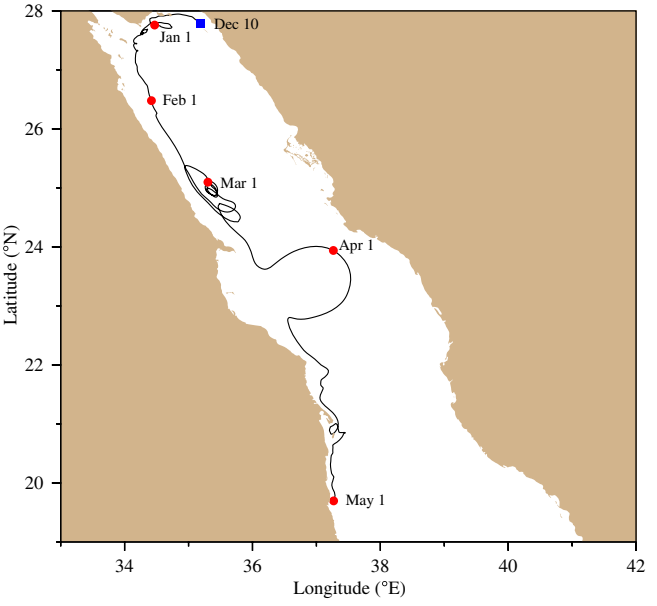

Figure 16. An example of the trajectory of a particle released in the northern end of the Red Sea for the period starting 10 December to 1 May in the successive year.

The combined effects of seasonal surface heat flux and basin-scale flow

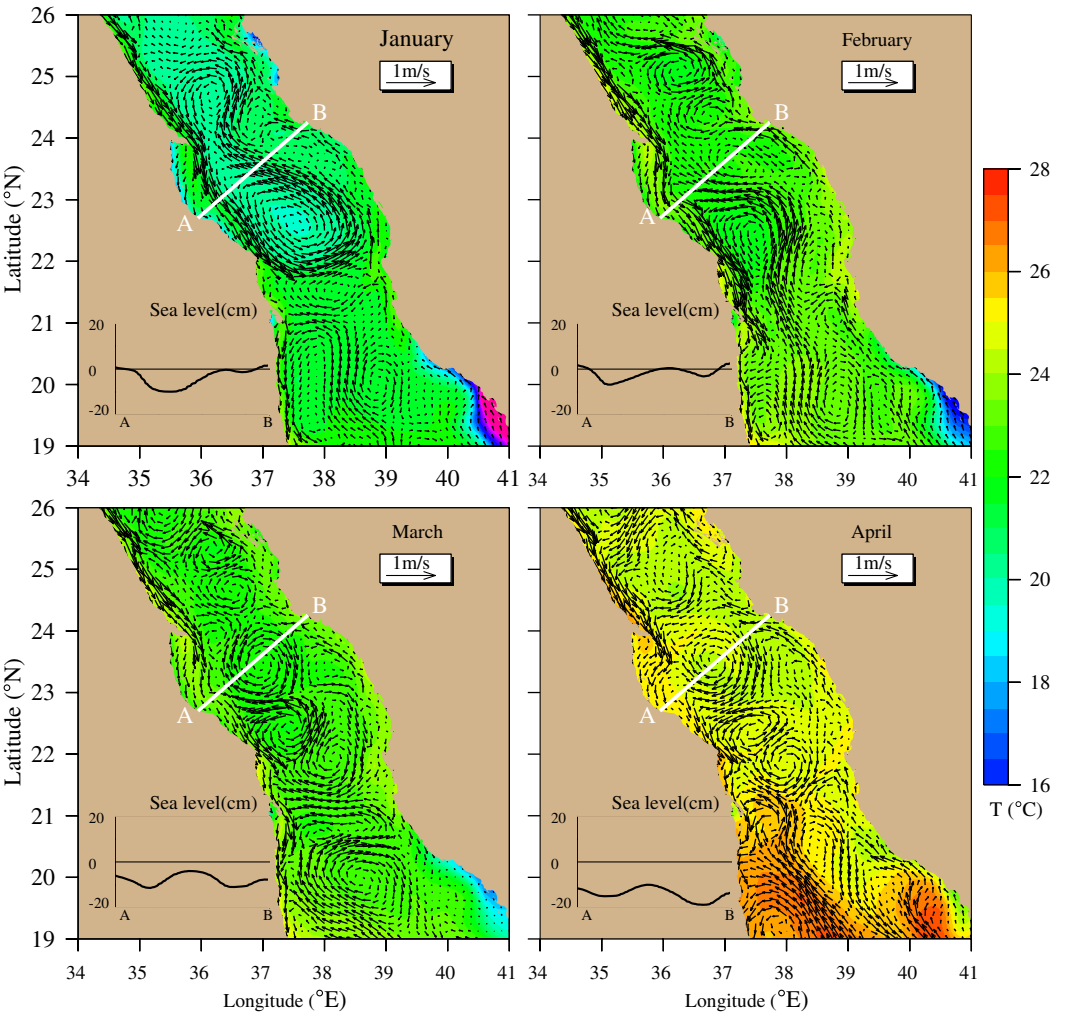

Figure 17. Sequences of the distributions of model-computed monthly averaged near-surface current vectors and water temperatures for January, February, March, and April. The results were from the same experiments shown in Figure 8, with a starting date of the simulation of 1 July in the previous year. (bottom left inset) Shows the distribution of sea level on the transect A–B. The distance between A and B was the same as that shown in Figure 8 with units of centimeters for the *y*-axis.

adjustment could be viewed more clearly in Figures 17 and 18, which show the monthly averaged flow fields and distributions of water density on the transect labeled A–B for January, February, March, and April, respectively. In January, in the region north of 21.5°N, the central Red Sea surface circulation was characterized by a cyclonic gyre (Figure 17, top left). This gyre seemed to originate from a well defined, southward coastal flow over the western shelf, which turned cyclonically around 21.5°N. This cyclonic gyre featured a concave sea level and cold-water zone in which the water was vertically well mixed in the upper 300 m (Figure 18, top left). The current in this gyre had its maximum speed at the surface and was distributed relatively uniformly in the upper mixed layer (Figure 18, top). In February, the southward coastal flow over the western shelf maintained its same magnitude and extended further south to 20.5°N while the cyclonic gyre separated into multiple cyclonic and anticyclonic mesoscale eddies (Figure 17, top right). A weak anticyclonic vortex appeared in the eastern region around 23.3°N, not far from where the drifter-detected eddy was located. Correspondingly, a convex sea level developed in the anticyclonic vortex zone. Vertical stratification in this month underwent little change compared to that in January: the water was still vertically well mixed in the upper 300 m (Figure 18, second row). In March, the anticyclonic vortex developed into a more prominent, circularly shaped eddy with relatively symmetric swirl velocities around the center (Figure 17, bottom left). The eddy was centered at the same location as the anticyclonic eddy detected by the drifters. During this month, the water temperature increased significantly near the surface as a result of surface heating, with warmer water inside the eddy (Figure 18, third row). In April, the thermocline was established

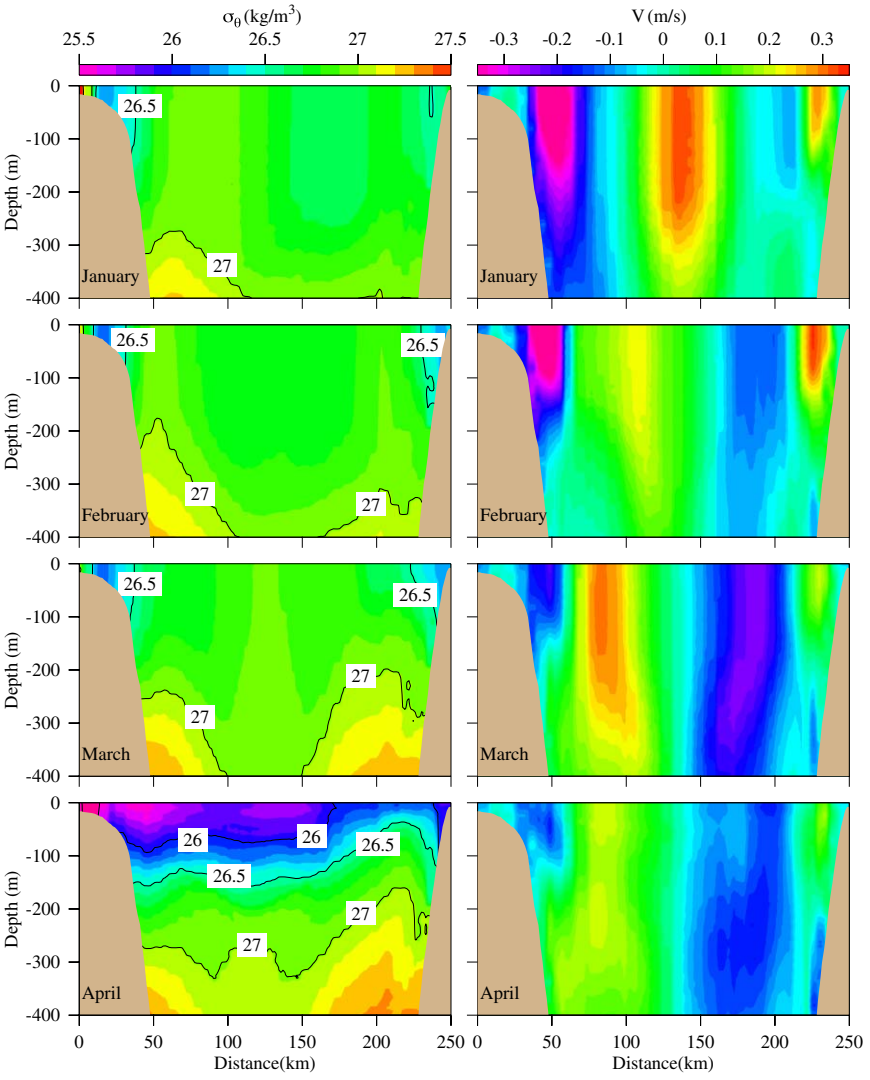

Figure 18. Sequences of the distributions of model-computed monthly averaged near-water temperatures (left) and along-isobath velocities on the transect A–B for January, February, March, and April. The results were from the same experiments shown in Figure 16.

around a depth of 100 m in the interior and outcropped over the eastern and western shelves (Figure 18, bottom). The eddy's shape and size remained similar and velocity became subsurface intensified (Figure 17, bottom right).

Two experimental results described as follows provide guidance here. First, when we forced the model with an initial condition of the monthly climatological T/S in March and integrated it for 2 months until May, the model did not produce the anticyclonic eddy in the area identified by the drifters. We repeated the experiments by shifting the initial state back to February but the model still did not produce the observed eddy. This suggests that the eddy did not form as a short-term adjustment of the oceanic responses to surface heating, so seasonal variation appears important. Second, our diagnostic experiments showed that the eddy could form in the condition with surface heat flux only. This suggests that the surface heat flux played a critical role in producing this eddy. Combining these two facts, we think that the seasonal adjustment of the flow to the surface heat flux played a key role in producing this eddy. An important aspect is that the stratification adjustment occurred in the vertical and across the shelf. Surface heating gradually built the cross-isobath temperature gradient over both eastern and western shelves. The southward flow over the western shelf was primarily wind driven, which did not change significantly over this period. However, the northward and cross-shelf coastal flow on the eastern shelf was closely related to the seasonal onset of the cross-isobath temperature gradient, which increased significantly with time.

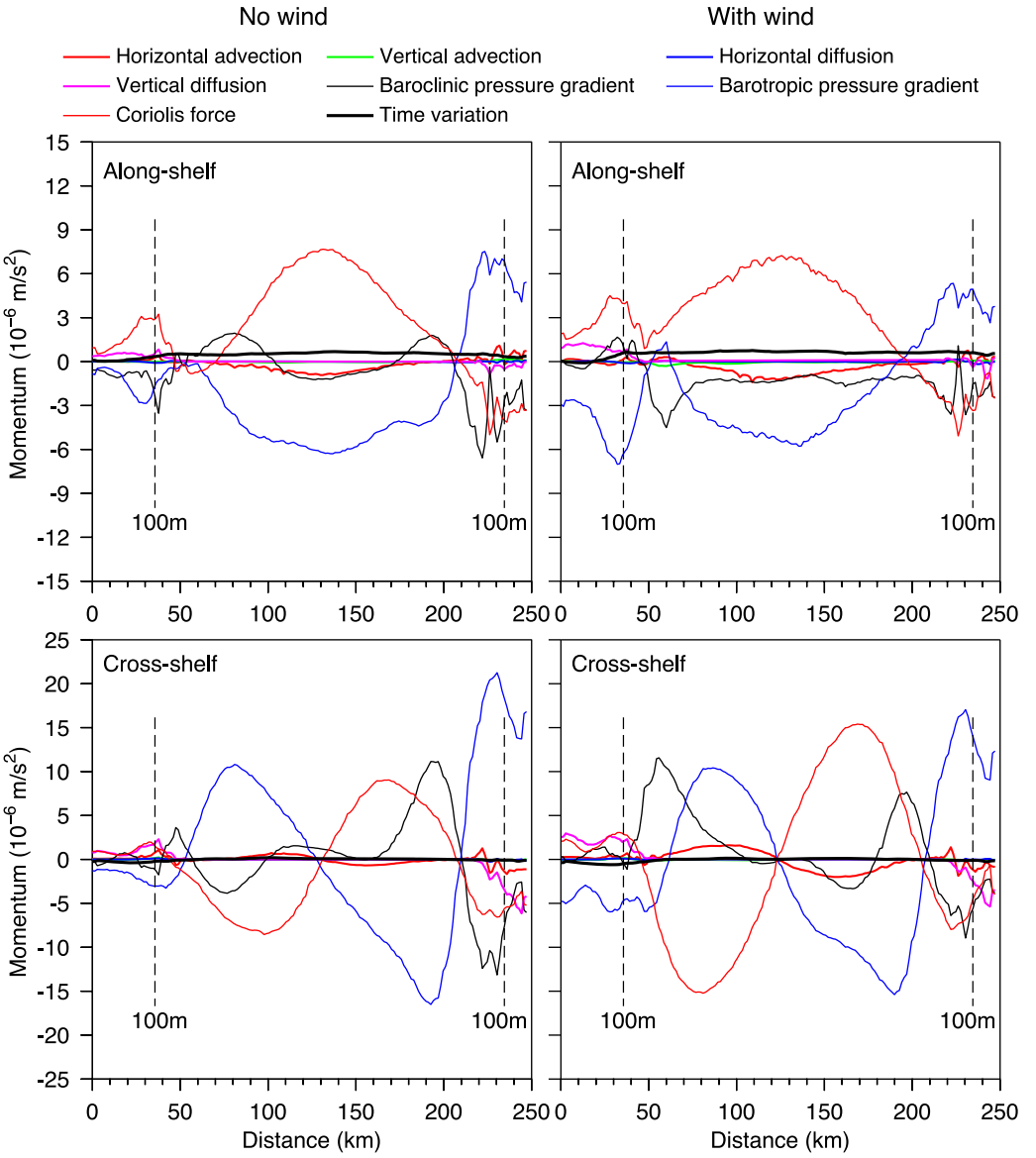

Figure 19. Cross-shelf distributions of vertically averaged terms in the along-shelf and cross-shelf momentum equations in the upper 400 m on the transect A–B for the cases without (left) and with (right) the inclusion of WRF wind forcing. The dashed line indicates the location where the water depth is 100 m.

6. Momentum Balances

We have examined the dynamical balance of the anticyclonic eddy and adjacent coastal currents for the cases without and with inclusion of wind forcing (Figure 19). Model-computed velocities were first transformed to the along-shelf and cross-shelf components and then the April monthly averaged value of each term in the momentum equations on the cross-eddy transect labeled A–B in Figure 9 was calculated. Defining the 100 m isobath as the shelfbreak that separates the interior and shelf, we found that the anticyclonic eddy was located in the interior with, to lowest order, a geostrophic balance in which the combined surface and baroclinic pressure gradient was balanced by the Coriolis force in both along-shelf and cross-shelf directions (Figure 19). This suggests that the response of the flow field to seasonal buoyancy forcing took place as an adjustment process regardless of the presence of wind forcing. The cross-shelf distributions and magnitudes of pressure gradients significantly differed in the cases without and with wind forcing. For the case without wind forcing, the cross-shelf baroclinic pressure gradient was distributed asymmetrically across the eddy, positive and larger on the eastern side and negative and smaller on the western side. Adding the wind forcing

significantly increased the baroclinic pressure gradient over the western side and thus intensified the northward flow of the eddy. The horizontal advection functioned as a first-order term and its contribution became bigger when the wind forcing was included. The eddy was not in steady state. Although the monthly averaged cross-shelf velocity in the interior was in nearly steady state, the along-shelf velocity was first-order term that changed slowly with time. Since both diffusion terms were small inside the eddy, the future development of this eddy was likely related to an interaction of this eddy flow with the surrounding eddy field.

In the regions shallower than 100 m, both eastern and western shelves featured northward and southward coastal flows, respectively. The transect A–B was not ideal to examine the momentum balance for these two flows since it was located in the transition zone between the anticyclonic eddy and these two coastal flows. Even so, the momentum balance in these shallow regions indicated that the flows there were driven by more complex nonlinear processes than the anticyclonic eddy in the interior.

7. Conclusions and Discussion

The unstructured-grid, Finite-Volume Community Ocean Model (FVCOM) was applied to examine the physical mechanisms for the formation of the anticyclonic eddy that was detected in the central Red Sea using surface drifters deployed in spring 2010. Driven by prescribed tidal elevation at the open boundary and atmospheric forcing at the sea surface, the model was capable of reproducing the observed anticyclonic eddy at the same location and with the same shape. Process-oriented modeling experiments were made to identify and quantify the key forcing that led to the eddy formation. The results suggest that this eddy can be formed as a result of flow adjustment to seasonal variability of buoyancy forcing. The overturning circulation produced by winter cooling spin up eddies by vortex stretching and squashing. Boundary currents are also modified as the overturning circulation over the whole Red Sea changes. The anticyclonic eddy is produced as a result of complex interactions between these features. Since forcing is solely due to surface buoyancy flux, the conversion of potential to kinetic energy is broadly important, but very difficult to attribute to the anticyclonic eddy. For one thing the formation time required was at least 3 months, which was associated with a southward coastal flow from the north over the western shelf. Although wind forcing was not a critical process in generating this eddy, it could significantly alter its location, intensity and structure. Wind-induced mixing could make this eddy flow subsurface intensified. The model experiments with two different T/S initial conditions were both capable of generating the observed anticyclonic eddy, suggesting that the primary physical mechanism proposed in this study was robust and insensitive to the initial T/S fields. Driven by the same forcing, however, the details of the mesoscale flow field in the central Red Sea could significantly differ for cases with different T/S initial conditions.

Momentum analysis indicates that the flow field in the anticyclonic eddy was approximately in geostrophic balance, with the surface and baroclinic pressure gradient forcing balanced by the Coriolis acceleration. Within this balance, the baroclinic pressure gradients were compatible to the surface pressure gradient forcing term, demonstrating that in addition to a barotropic response of the flow to the sea level change, a baroclinic response to surface buoyancy forcing also played a key role in the eddy formation. Horizontal advection functioned as a first order of magnitude term and its contribution increased as wind forcing was included. The eddy evolved slowly in time but did not reach steady state on a monthly time scale. The momentum analysis also suggests that the flow over the shallow eastern and western shelves was driven by more complex nonlinear processes than the anticyclonic eddy in the interior.

It should be pointed out here that the magnitude of the model-predicted eddy flow was weaker than the drifter-derived velocity. One possible reason is related to vertical stratification. The CTD/ADCP survey carried out in April 2010 indicated a sharp thermocline in a depth range of 50–200 m, with a thin surface mixed layer in the upper 50 m. Although the model predicted similar vertical stratification in the interior, it seemed to overestimate vertical mixing over the rapidly changing slope. This overestimation was likely related to the initial T/S field specified in the model and vertical model resolution. Since our focus was on the physical mechanisms for the eddy formation rather than on attempting a realistic hindcast for a specific time period, we have not made a further examination of this aspect. This issue, however, must be taken into account if one plans to establish a real-time simulation model for the Red Sea.

Our studies were focused on the diagnostic analysis of the forcing driving the eddy formation. It remains unanswered whether or not this eddy could be produced by baroclinic instability of the southward coastal

current that developed gradually over the seasons. *Chen et al.* [2001] applied the energy transfer theory to examine the formation of an eddy resulting from the instability of the Keweenaw Current in Lake Superior where a permanent thermal front developed during the summer. *Badin et al.* [2009] and *Holt and Umlauf* [2008] used similar approaches to investigate the instability and eddy formation of tidal mixing fronts in the North Sea, where a well-defined tidal mixing front existed. In these two coastal systems, the mean frontal flow could be well defined, and both barotropic and baroclinic instability criteria could be directly applied to estimate the stability of the current jet. In the Red Sea, however, the eddy formation occurred as a result of a long-term, basin-scale adjustment of flow field and stratification to surface forcing. Since the region is so narrow, the eddy formed with the flow from both western and eastern coasts. It is not easily attributed to the instability of the coastal current along a single coast. Since the observed eddy was evident in the same region in other years (see Figure 4), the existence of this eddy may be related to coastline geometry in subtle ways. For this reason, we were unable to come up with a clean procedure for conducting an instability analysis, in terms of either growth rate/wavelength or energy analysis. However, such an analysis might be feasible within the context of a more idealized model and we may pursue this in the future as a separate follow-up paper.

Appendix A: Tidal Simulations With Comparisons to ADCIRC

RS-FVCOM was configured using high-resolution bathymetric data provided by Dr. Ewa Jarosz at the Naval Research Laboratory (NRL), Stennis Space Center, Mississippi, USA. The sources of this bathymetry data were (1) the Digital Bathymetric Data Base-Variable Resolution (DBDB-V) and (2) charts issued by the Defense Mapping Agency [*Jarosz et al.*, 2005]. This bathymetry was used for the NRL ADCIRC tidal model for

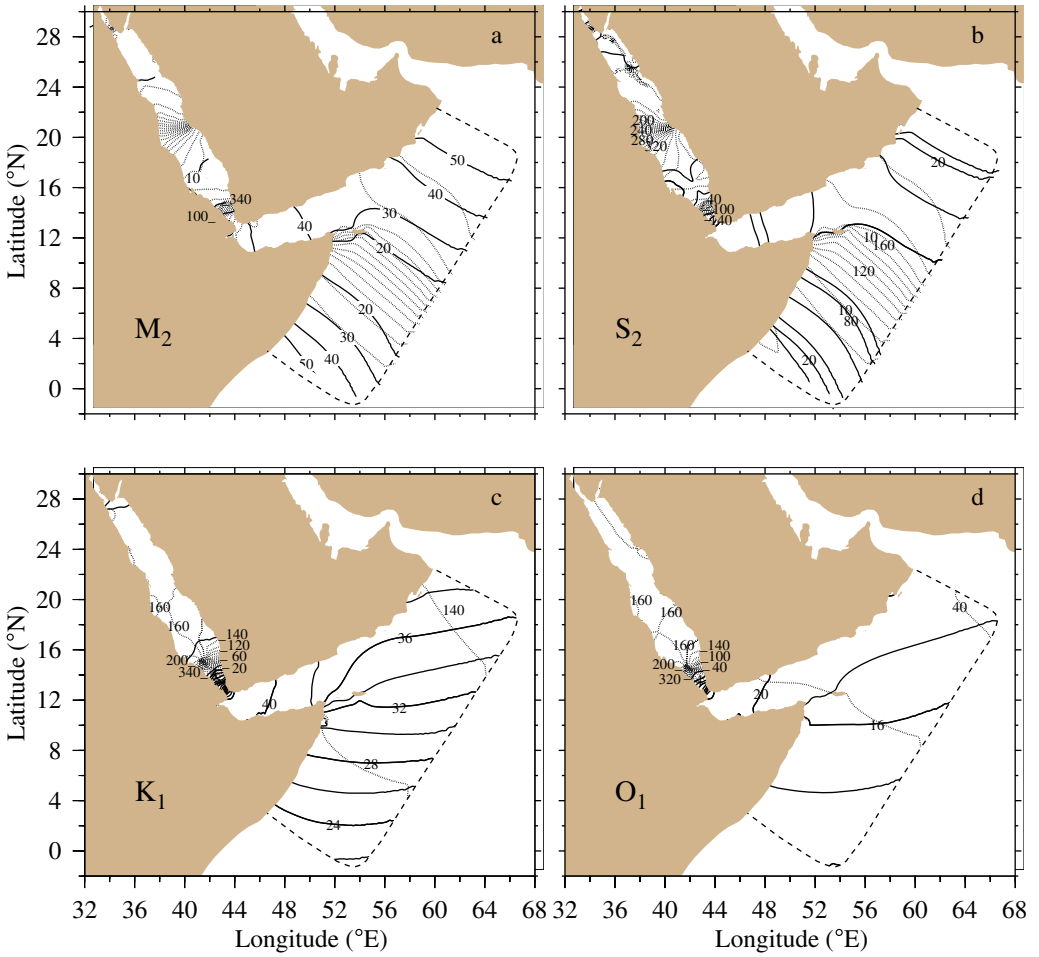

Figure A1. Distributions of coamplitudes (solid lines) and cophases (dashed lines) of model-computed M_2, S_2, K_1, and O_1 tidal constituents.

Table A1. Correlation Coefficients, Standard Deviations, and *H*-Values Estimated by the Comparison Between RS-FVCOM-Computed and Observed Tidal Amplitudes and Phases at 33 Tidal Gauges

	Correlation Coefficient		Standard Deviation		
Tidal Constituent	Amplitude	Phase	Amplitude (cm)	Phase (°)	*H* (cm)
M_2	0.82	0.88	9.43	36.23	10.03
S_2	0.95	0.95	2.14	28.57	3.00
K_1	0.99	0.99	2.18	15.47	2.11
O_1	0.99	0.99	0.88	12.37	1.08

the Red Sea. The tide in RS-FVCOM was simulated by driving the model using tidal elevation consisting of eight tidal constituents (M_2, S_2, N_2, K_2, K_1, P_1, and O_1) on the open boundary. The tidal simulation results were validated by comparisons with tidal constants (amplitudes and phases) of the four major tidal constituents (M_2, S_2, P_1, and O_1) at all tidal gauges and also with the ADCIRC results. The comparison results of RS-FVCOM with tidal data and ADCIRC are briefly summarized below.

Figure A1 shows the computed cotidal charts of M_2, S_2, K_1, and O_1 tidal constituents in the entire computational domain. When configured with the same bathymetric data, RS-FVCOM produced coamplitude and cophase patterns almost identical with the ADCIRC results published by *Jarosz et al*. [2005]. For the M_2 and S_2 constituents, two counter-clockwise amphidromic points were located at approximately 42.9°E, 13.8°N and 38.8°E, 20.5°N respectively. For the O_1 and K_1 constituents, one anticlockwise amphidromic point was located at approximately 41.8°E, 15.0°N. Both RS-FVCOM and ADCIRC cotidal charts are in good agreement with *Defant* [1961].

The RS-FVCOM-computed tidal amplitudes and phases of M_2, S_2, K_1, and O_1 tidal constituents were compared with observational data at 33 tidal gauges. In addition to estimating the root-square mean error, we also computed an average difference between computed and observed tides following the method used in *Davies et al*. [1997]. Denoting *H* to be this averaged difference, it can be calculated by the formula

$$H=\frac{1}{N}\sum_{k=1}^{N}\sqrt{\left(A_{obs}\cos g_{obs}-A_{com}\cos g_{com}\right)^2+\left(A_{obs}\sin g_{obs}-A_{com}\sin g_{com}\right)^2} \tag{A1}$$

where *N* is the number of tidal gauges and letters "A" and "g" represent amplitude and phase, respectively. The subscripts "*obs*" and "*com*" refer to the observed and computed values. Table A1 shows the correlation coefficient, standard deviation, and *H* values summarized for model-data comparison for M_2, S_2, K_1, and O_1 tidal constituents at 44 tidal gauges. The correlation coefficients between computed and observed M_2 tidal amplitudes and phases were 0.82 and 0.88, with an *H* value of 10.03 cm. The correlation coefficients between computed and observed amplitudes and phases for S_2, K_1, and O_1 tidal constituents were greater than 0.9, with *H* values < 3 cm. These values show no significant difference from the ADCIRC results. RS-FVCOM showed smaller errors than ADCIRC at some stations, but larger errors at other stations. After averaging, they are at the same accuracy level. The relatively large errors in phase shown in both RS-FVCOM and ADCIRC were probably due to the inaccurate representation of local bathymetry around tidal gauges.

Acknowledgments

This project was supported by the King Abdullah University of Science and Technology (KAUST). The development of Global-FVCOM was supported by NSF grants ARC0712903, ARC0732084, ARC0804029 and OCE-1203393. C. Chen's contributions were also supported by the International Center for Marine Studies at Shanghai Ocean University through the "Shanghai Universities First-class Disciplines Project." L. Pratt was also supported by National Science Foundation Grant OCE0927017. We thank Ewa Jarosz at the Naval Research Laboratory who provided us the high-resolution bathymetric data of the Red Sea. That data were used to set up the ARCIRC and FVCOM grids in that region. Comments and suggestions from two anonymous reviewers were thoughtful and valuable and helped us improve this manuscript.

References

Assaf, G., and D. Anati (1974), Stress distribution in the Red Sea and in the Gulf of Aqaba, *J. Phys. Oceanogr.*, *4*, 663–668.

Badin, G., R. G. Williams, J. T. Holt, and L. J. Fernand (2009), Are mesoscale eddies in shelf seas formed by baroclinic instabilities of tidal fronts?, *J. Geophys. Res.*, *114*, C10021, doi:10.1029/2009JC005340.

Beal, L. M., A. Ffield, and A. L. Gordon (2000), Spreading of Red Sea overflow waters in the Indian Ocean, *J. Geophys. Res.*, *105C*, 8549–8564.

Bower, A. S., H. D. Hunt, and J. F. Price (2000), Character and dynamics of the Red Sea and Persian Gulf outflow, *J. Geophys. Res.*, *105*(C3), 6387–6414, doi:10.1029/1999JC900297.

Bower, A. S., D. M. Frantantoni, W. E. Johns, and H. Peters (2002), Gulf of Aden eddies and their impact on Red Sea water, *Geophys. Res. Lett.*, *29*(21), 2025, doi:10.1029/2002GL015342.

Bower, A. S., W. E. Johns, D. M. Frantantoni, and H. Peters (2005), Equilibration and circulation of Red Sea outflow water in the western Gulf of Aden, *J. Phys. Oceanogr.*, *35*, 1963–1985.

Chen, C., J. Zhu, E. Ralph, S. A. Green, J. W. Budd, and F. Y. Zhang (2001), Prognostic modeling studies of the Keweenaw Current in Lake Superior, part I: Formation of evolution, *J. Phys. Oceanogr.*, *31*, 379–395.

Chen, C., H. Liu, and R. C. Beardsley (2003), An unstructured grid, finite-volume, three-dimensional, primitive equations ocean model: Application to coastal ocean and estuaries, *J. Atmos. Oceanic Technol.*, *20*(1), 159–186.
Chen, C., R. C. Beardsley, and G. Cowles (2006a), An unstructured grid, finite-volume coastal ocean model (FVCOM) system, Special Issue entitled "Advances in Computational Oceanography," *Oceanography*, *19*(1), 78–89.
Chen, C., G. Cowles, and R. C. Beardsley (2006b), An unstructured-grid, finite-volume coastal ocean model: FVCOM User Manual, 2nd ed., *SMAST/UMASSD Tech. Rep. 06–0602*, 315 pp., Univ. Mass.-Dartmouth, Dartmouth, Mass.
Chen, C., R. C. Beardsley, G. Cowles, J. Qi, Z. Lai, G. Gao, D. Stuebe, Q. Xu, P. Xue, J. Ge, R. Ji, S. Hu, R. Tian, H. Huang, L. Wu, and H. Lin (2012), An unstructured-grid, finite-volume community ocean model FVCOM user manual, 3rd ed., *SMAST/UMASSD Tech. Rep. 11-1101*, 373 pp., Univ. Mass.-Dartmouth, Dartmouth, Mass.
Davies, A. M., S. C. M. Kwong, and R. A. Flather (1997), A three-dimensional model of diurnal and semi diurnal tides on the European shelf, *J. Geophys. Res.*, *102*, 8625–8656.
Defant, A. (1961), *Physical Oceanography*, vol. 1, 598 pp., Pergamon, Oxford, U. K.
Egbert, G. D., and S. Y. Erofeeva (2002), Efficient inverse modeling of barotropic ocean tides, *J. Atmos. Oceanic Technol.*, *19*(2), 183–204, doi:10.1175/1520-0426 (2002)019<0183:EIMOBO>2.0.CO;2.
Eshel, G., and N. H. Haik (1997), Climatological coastal jet collision, intermediate water formation, and the general circulation of the Red Sea, *J. Phys. Oceanogr.*, *27*, 1233–1257.
Gao, G., C. Chen, J. Qi, and R. C. Beardsley (2011), An unstructured-grid, finite-volume sea ice model: Development, validation, and application, *J. Geophys. Res.*, *116*, C00D04, doi:10.1029/2010JC006688.
Gent, P. R., and M. A. Cane (1989), A reduced gravity, primitive equation model of the upper equatorial ocean, *J. Comput. Phys.*, *81*, 444–480.
Huang, H., C. Chen, G. W. Cowles, C. D. Winant, R. C. Beardsley, K. S. Hedstrom, and D. B. Haidvogel (2008), FVCOM validation experiments: Comparisons with ROMS for three idealized barotropic test problems, *J. Geophys. Res.*, *113*, C07042, doi:10.1029/2007JC004557.
Holt, J. T., and L. Umlauf (2008), Modelling the tidal mixing fronts and seasonal stratification of the northwest European continental shelf, *Cont. Shelf Res.*, *28*, 887–903.
Jarosz, E., C. A. Blain, S. P. Murray, and M. Inoue (2005), Barotropic tides in the Bab el Mandab Strait—Numerical simulations, *Cont. Shelf Res.*, *25*, 1225–1247.
Jiang, H., J. T. Farrar, R. C. Beardsley, R. Chen, and C. Chen (2009), Zonal surface wind jets across the Red Sea due to mountain gap forcing along both sides of the Red Sea, *Geophys. Res. Lett.*, *36*, L19605, doi:10.1029/2009GL04008.
Maillard, C., and G. Soliman (1986), Hydrography of the Red Sea and exchange with the Indian Ocean in summer, *Oceanol. Acta*, *9*, 249–269.
Matt, S., and W. E. Johns (2007), Transport and entrainment in the Red Sea outflow plume, *J. Phys. Oceanogr.*, *37*, 819–836.
Mellor, G. L., and T. Yamada (1982), Development of a turbulence closure model for geophysical fluid problem, *Rev. Geophys. Space Phys.*, *20*, 851–875.
Özgökmen, Y. M., W. E. Johns, H. Peters, and S. Matt (2003), Turbulent mixing in the Red Sea outflow plume from a high-resolution nonhydrostatic model, *J. Phys. Oceanogr.*, *33*, 1846–1869.
Phillips, O. M. (1966), On turbulent convection currents and the circulation of the Red Sea, *Deep Sea Res. Oceanogr. Abstr.*, *13*, 1149–1160.
Pratt, L. J., W. Johns, S. P. Murray, and K. Katsumata (1999), Hydraulic interpretation of direct velocity measurements in the Bab al Mandab, *J. Phys. Oceanogr.*, *29*(11), 2769−2784.
Pratt, L. J., H. E. Deese, S. P. Murray, and W. Johns (2000), Continuous dynamical modes in straits having arbitrary cross sections, with applications to the Bab al Mandab, *J. Phys. Oceanogr.*, *30*(10), 2515−2534.
Quadfasel, D., and H. Baunder (1993), Gyre-scale circulations cells in the Red Sea, *Oceanol. Acta*, *16*(3), 221–229.
Smagorinsky, J. (1963), General circulation experiments with the primitive equations, I. The basic experiment, *Mon. Weather Rev.*, *91*, 99–164.
Sofianos, S. S., and W. E. Johns (2001), Wind induced sea level variability in the Red Sea, *Geophys. Res. Lett.*, *28*, 3175–3178.
Sofianos, S. S., and W. E. Johns (2002), An oceanic general circulation model (OGCM) investigation of the Red Sea circulation: 1. Exchange between the Red Sea and the Indian Ocean, *J. Geophys. Res.*, *107*(C11), 3196, doi:10.1029/2001JC00184.
Sofianos, S. S., and W. E. Johns (2003), An oceanic general circulation model (OGCM) investigation of the Red Sea circulation: 2. Three-dimensional circulation in the Red Sea, *J. Geophys. Res.*, *108*(C3), 3066, doi:10.1029/2001JC00185.
Tragou, E., and C. Garrett (1997), The shallow thermohaline circulation of the Red Sea, *Deep Sea Res., Part I*, *44*, 1355–1376.
Tragou, E., C. Garrett, R. Outerbridge, and C. Gilman (1999), The heat and freshwater budgets of the Red Sea, *J. Phys. Oceanogr.*, *29*, 2504–2521.
Trommer, G., M. Siccha, E. J. Rohling, K. Grant, M. T. J. van der Meer, S. Schouten, C. Hemleben, and M. Kurcera (2010), Mlllennial-scale variability in Red Sea circulation in response to Holocene insolation forcing, *Paleoceanography*, *25*, PA3203, doi:10.1029/2009PA001926.
Winant, C. D. (2004), Three-dimensional wind-driven flow in an elongated, rotating basin, *J. Phys. Oceanogr.*, *34*, 462–476, doi:10.1175/1520-0485.
Xue, P., C. Chen, R. C. Beardsley, and R. Limeburner (2011), Observing system simulation experiments with ensemble Kalman filters in Nantucket Sound, Massachusetts, *J. Geophys. Res.*, *116*, C01011, doi:10.1029/2010JC006428.
Zhai, P., and A. Bower (2013), The response of the Red Sea to a strong wind jet near the Tokar Gap in summer, *J. Geophys. Res.*, *118*(1), 421–434, doi:10.1029/2012JC008444.